J. Plasma Phys. (2020), *vol*. 86, 905860601
Published by Cambridge University Press
doi:10.1017/S0022377820001294

Stabilisation of short-wavelength instabilities by parallel-to-the-field shear in long-wavelength $E \times B$ flows

M. R. Hardman [1,2,†], **M. Barnes** [1] **and C. M. Roach** [2]

[1]Rudolf Peierls Centre for Theoretical Physics, University of Oxford, Oxford OX1 3PU, UK

[2]Culham Centre for Fusion Energy, UKAEA, Abingdon OX14 3DB, UK

(Received 7 July 2020; revised 15 September 2020; accepted 16 September 2020)

Magnetised plasma turbulence can have a multiscale character: instabilities driven by mean temperature gradients drive turbulence at the disparate scales of the ion and the electron gyroradii. Simulations of multiscale turbulence, using equations valid in the limit of infinite scale separation, reveal novel cross-scale interaction mechanisms in these plasmas. In the case that both long-wavelength (ion-gyroradius-scale) and short-wavelength (electron-gyroradius-scale) linear instabilities are driven far from marginal stability, we show that the short-wavelength instabilities are suppressed by interactions with long-wavelength turbulence. Two novel effects contributed to the suppression: parallel-to-the-field-line shearing by the long-wavelength $\boldsymbol{E} \times \boldsymbol{B}$ flows, and the modification of the background density gradient by the piece of the long-wavelength electron adiabatic response with parallel-to-the-field-line variation. In contrast, simulations of multiscale turbulence where instabilities at both scales are driven near marginal stability demonstrate that when the long-wavelength turbulence is sufficiently collisional and zonally dominated the effect of cross-scale interaction can be parameterised solely in terms of the local modifications to the mean density and temperature gradients. We discuss physical arguments that qualitatively explain how a change in equilibrium drive leads to the observed transition in the impact of the cross-scale interactions.

Key words: plasma nonlinear phenomena, plasma simulation, fusion plasma

1. Introduction

In a magnetised plasma, gradients in the mean temperature of the component particle species act as sources of free energy that drive instability. Instabilities saturate through nonlinear interactions to form turbulence; the nature of the turbulence is determined by the character of the underlying instabilities. In this paper, we consider the effect of cross-scale nonlinear interactions in turbulence driven at the well-separated space–time scales associated with ion and electron dynamics, respectively. This represents a fundamentally different system to that usually employed in turbulence studies, which consists of a single injection range, a single inertial range and a single dissipation range.

† Email address for correspondence: michael.hardman@physics.ox.ac.uk

Instabilities in magnetised plasmas typically have a structure that is elongated along field lines; this is a result of the Lorentz force, which causes particles to perform gyro orbits in the plane perpendicular to the magnetic field line, whilst allowing unimpeded motion in the parallel-to-the-field direction. By definition, in a magnetised plasma the typical particle gyroradius is much smaller than the device scale a that determines the parallel-to-the-field scale of instabilities. In the core of magnetic confinement fusion devices two of the dominant instabilities which drive turbulence are the ion temperature gradient (ITG) and the electron temperature gradient (ETG) instabilities (Lee *et al.* 1987; Horton, Hong & Tang 1988; Romanelli 1989; Cowley, Kulsrud & Sudan 1991). The ITG instability drives turbulence at the scale of the ion thermal gyroradius $\rho_{\mathrm{th},i}$, at frequencies of the order of the ion transit frequency $v_{\mathrm{th},i}/a$, with $v_{\mathrm{th},i}$ the ion thermal speed. The ETG instability drives turbulence at the scale of the electron thermal gyroradius $\rho_{\mathrm{th},e}$, at frequencies of the order of the electron transit frequency $v_{\mathrm{th},e}/a$, with $v_{\mathrm{th},e}$ the electron thermal speed.

When the ion and electron temperatures are approximately equal the space and time scales associated with the ETG and ITG instabilities can be well separated: the separation of scales is determined by the square root of the electron-to-ion mass ratio $(m_e/m_i)^{1/2} \sim \rho_{\mathrm{th},e}/\rho_{\mathrm{th},i} \sim v_{\mathrm{th},i}/v_{\mathrm{th},e}$. For the deuterium ions commonly used in magnetic confinement fusion, the small value of $(m_e/m_i)^{1/2} \approx 1/60$ allows for the possibility that two distinct types of turbulence coexist at disparate space–time scales. This possibility has sparked considerable interest in multiscale turbulence, see, e.g., Maeyama *et al.* (2015, 2017*a*); Maeyama, Watanabe & Ishizawa (2017*b*), Howard *et al.* (2014, 2015, 2016*a*,*b*), Bonanomi *et al.* (2018), Görler & Jenko (2008), Candy *et al.* (2007), Waltz, Candy & Fahey (2007), Staebler *et al.* (2016, 2017), Creely *et al.* (2019) and Itoh & Itoh (2001).

Direct numerical simulations (DNS) of multiscale plasma turbulence show that the interactions between long-wavelength and short-wavelength scales can be important for determining the character of the turbulence and the flux of heat exhausted from the fusion plasma (Maeyama *et al.* 2015, 2017*a*; Howard *et al.* 2016*a*,*b*). The small value of $(m_e/m_i)^{1/2}$ makes DNS of multiscale plasma turbulence extremely challenging; the increased cost of multiscale DNS compared with conventional simulations scales with $(m_i/m_e)^{3/2}$. Recent multiscale DNS have been performed using the electron-to-deuterium mass ratio (e.g. Howard *et al.* 2016*a*,*b*; Bonanomi *et al.* 2018) and electron-to-hydrogen mass ratio (e.g. Maeyama *et al.* 2015, 2017*a*). The multiscale DNS provide evidence showing that the presence of short-wavelength turbulence can sometimes modestly enhance long-wavelength, ITG-driven fluxes (Maeyama *et al.* 2015, 2017*a*; Howard *et al.* 2016*a*,*b*). In contrast, multiscale DNS of microtearing mode (MTM) turbulence show that the presence of short-wavelength ETG modes can suppress the long-wavelength MTM (Maeyama *et al.* 2017*b*). Most relevant to the results presented in this paper, the multiscale DNS give clear evidence that shows that short-wavelength turbulence can be suppressed in the presence of long-wavelength turbulence as a result of cross-scale interaction (Maeyama *et al.* 2015, 2017*a*; Howard *et al.* 2016*b*).

In this paper, we use numerical simulations of scale-separated turbulence to demonstrate the effect of long-wavelength turbulence on short-wavelength fluctuations. We show that strongly driven, long-wavelength turbulence can stabilise the short-wavelength ETG instability through cross-scale interaction. We show that this stabilisation is due to two effects: the parallel-to-the-field shearing of short-wavelength fluctuations by long-wavelength $\boldsymbol{E} \times \boldsymbol{B}$ drifts; and the modification of the background drives of instability by gradients of long-wavelength fluctuations. We show that the modification to the background drives can be characterised as having two main components: a

perturbed Maxwellian piece that shifts the mean density and temperature gradients by a constant value; and a density gradient due to the long-wavelength electron adiabatic response that varies in the parallel-to-the-field direction. These mechanisms may explain the suppression of the short-wavelength modes observed in DNS of strongly driven turbulence. We show that parallel-to-the-field shearing can be a significant cross-scale interaction mechanism far above marginal stability, but that it can be less important in turbulence driven near marginal stability. We examine one example of near-marginal turbulence where we find that the effect of cross-scale interaction on the ETG instability can be described with the local modification of the density and temperature gradient length scales by gradients of long-wavelength fluctuations.

2. Scale-separated model

The local, δf gyrokinetic equations describe the evolution of magnetised plasma turbulence driven by mean gradients in the limit that $\rho_{\mathrm{th},i}/a \to 0$ and $\rho_{\mathrm{th},e}/a \to 0$ (Catto 1978; Frieman & Chen 1982; Brizard & Hahm 2007); this model is the starting point in the derivation of scale-separated equations for multiscale, electrostatic turbulence (Hardman *et al.* 2019). We now briefly review this derivation, first presented in Hardman *et al.* (2019). Ultimately, we find that the local gradients of slowly evolving, long-wavelength turbulence act to modify the mean gradients and flows which drive (or suppress) rapidly evolving, short-wavelength fluctuations. In analogy to the coupling between turbulence and large-scale transport (Sugama & Horton 1997; Abel *et al.* 2013), we might expect short-wavelength turbulence to generate fluxes that diffuse long-wavelength turbulence. However, this effect is small by $(m_e/m_i)^{1/2}$ in the ordering, and hence too small to appear at leading order in the $(m_e/m_i)^{1/2}$ expansion that we employ.

In the limit that $(m_e/m_i)^{1/2} \to 0$, multiscale turbulence can be meaningfully decomposed into components: the long-wavelength 'ion scale' (IS) and the short-wavelength 'electron scale' (ES). We assume that IS turbulence varies only on $\rho_{\mathrm{th},i}$ perpendicular-to-the-field scales in space and on $a/v_{\mathrm{th},i}$ scales in time, whereas ES turbulence has much finer $\rho_{\mathrm{th},e}$ perpendicular-to-the-field structures, and evolves on the rapid $a/v_{\mathrm{th},e}$ time scale. Both IS and ES turbulence have parallel-to-the-field scales of order a. Here, $\rho_{\mathrm{th},p} = v_{\mathrm{th},p}/\Omega_p$, with p the particle species index, $v_{\mathrm{th},p} = \sqrt{2T_p/m_p}$, $\Omega_p = Z_p eB/m_p c$ the species cyclotron frequency, T_p the species temperature, Z_p the species charge number, e the elementary electric charge, B the magnetic field strength and c the speed of light. The distribution function δf and electrostatic potential ϕ of the turbulence are sums of the IS and ES components:

$$\delta f = \overline{\delta f} + \widetilde{\delta f}, \quad \phi = \bar{\phi} + \tilde{\phi}, \tag{2.1a,b}$$

where $\bar{\chi}$ and $\tilde{\chi}$ are the IS and ES pieces of any quantity χ, respectively. To carry out this decomposition, we introduce the ES average $\langle\cdot\rangle^{\mathrm{ES}}$, an average over $\rho_{\mathrm{th},e}$ perpendicular-to-the-field scales and $a/v_{\mathrm{th},e}$ times. We assume that ES turbulence is statistically periodic on $\rho_{\mathrm{th},e}$ scales, i.e. $\langle\widetilde{\delta f}\rangle^{\mathrm{ES}} = 0$. This allows us to use $\langle\cdot\rangle^{\mathrm{ES}}$ to extract the scale-separated, coupled gyrokinetic equations for $\overline{\delta f}$ and $\widetilde{\delta f}$ from the gyrokinetic equations for δf.

The IS component of the turbulence is evolved with the usual gyrokinetic equation for the ion species, and a parallel-orbit-averaged equation for the electron species. The IS turbulence evolves independently of the ES turbulence to leading order in the $(m_e/m_i)^{1/2}$ expansion. At the ES the ion species have a Boltzmann response. The evolution of the ES turbulence is governed by the short-wavelength electron gyrokinetic equation

(Hardman *et al.* 2019)

$$\left(\frac{\partial}{\partial t}+\bar{\boldsymbol{v}}_E\cdot\boldsymbol{\nabla}\right)\tilde{g}+v_\parallel\boldsymbol{b}\cdot\boldsymbol{\nabla}\theta\frac{\partial\tilde{g}}{\partial\theta}+(\boldsymbol{v}_M+\tilde{\boldsymbol{v}}_E)\cdot\boldsymbol{\nabla}\tilde{g}+\tilde{\boldsymbol{v}}_E\cdot(\boldsymbol{\nabla}F_0+\boldsymbol{\nabla}\bar{g})$$
$$=\frac{eF_0}{T_e}\left(v_\parallel\boldsymbol{b}\cdot\boldsymbol{\nabla}\theta\frac{\partial\tilde{\varphi}}{\partial\theta}+\boldsymbol{v}_M\cdot\boldsymbol{\nabla}\tilde{\varphi}\right)+\tilde{C}, \tag{2.2}$$

where we express the ES gyrokinetic equation in terms of the particle guiding centre $\boldsymbol{R}=\boldsymbol{r}-\boldsymbol{b}\times\boldsymbol{v}/\Omega_e$, with $\boldsymbol{r}$ the particle position, $\boldsymbol{b}$ the magnetic field direction, $\boldsymbol{v}$ the particle velocity; ε the particle kinetic energy; $\lambda=\mu/\varepsilon$ the pitch angle, with μ the magnetic moment; σ the sign of the particle velocity in the magnetic field direction $v_\parallel=\boldsymbol{v}\cdot\boldsymbol{b}=\sigma(2\varepsilon/m_p)^{1/2}(1-\lambda B)^{1/2}$; the gyroaveraged ES potential $\tilde{\varphi}=\langle\tilde{\phi}\rangle^\vartheta$, with ϑ the angle of gyration about $\boldsymbol{b}$ and $\langle\cdot\rangle^\vartheta$ the electron gyroaverage at fixed $\boldsymbol{R}$; the ES gyroaveraged electron distribution function $\tilde{g}=\langle\widetilde{\delta f}_e\rangle^\vartheta=\tilde{h}+e\tilde{\varphi}F_0/T_e$, with $\widetilde{\delta f}_e(\boldsymbol{r})=\tilde{h}(\boldsymbol{R})+e\tilde{\phi}(\boldsymbol{r})F_0/T_e$, $\tilde{h}$ the non-Boltzmann part of the ES electron distribution function and F_0 the Maxwellian electron mean distribution function. The poloidal angle θ is the parallel-to-the-field coordinate; $\boldsymbol{v}_M$ is the electron magnetic drift; and $\tilde{C}$ accounts for the effects of collisions on $\tilde{g}$. The long-wavelength and short-wavelength $\boldsymbol{E}\times\boldsymbol{B}$ drifts are $\bar{\boldsymbol{v}}_E=(c/B)\boldsymbol{b}\times\boldsymbol{\nabla}\bar{\phi}$ and $\tilde{\boldsymbol{v}}_E=(c/B)\boldsymbol{b}\times\boldsymbol{\nabla}\tilde{\varphi}$, respectively; and $\bar{g}=\overline{\delta f}_e$ is the long-wavelength, IS, electron distribution function. Gyroaverages do not appear in the definitions of $\bar{\boldsymbol{v}}_E$ or $\boldsymbol{\nabla}\bar{g}$ as $\rho_{\mathrm{th},e}$ is much smaller than the spatial scale of the IS structures. Equation (2.2) is closed by the ES quasineutrality relation $Z_i\tilde{n}_i=\tilde{n}_e$, with $\tilde{n}_p$ the ES fluctuating density of species p. The ES quasineutrality relation can be written

$$\int\mathrm{d}^3\boldsymbol{v}|_{\boldsymbol{r}}\left(\tilde{g}(\boldsymbol{R})+\frac{eF_0}{T_e}(\tilde{\phi}(\boldsymbol{r})-\tilde{\varphi}(\boldsymbol{R}))\right)=-\frac{Z_ie\tilde{\phi}(\boldsymbol{r})}{T_i}n_{0e}, \tag{2.3}$$

where n_{0e} is the mean electron density, and the subscript $\boldsymbol{r}$ on the volume element in the velocity space integral indicates that the integral is to be taken at fixed particle position.

Cross-scale interaction is mediated by the terms $\bar{\boldsymbol{v}}_E\cdot\boldsymbol{\nabla}\tilde{g}$ and $\tilde{\boldsymbol{v}}_E\cdot\boldsymbol{\nabla}\bar{g}$ in the electron gyrokinetic equation, (2.2). The gradient $\boldsymbol{\nabla}\bar{g}$ and the drift $\bar{\boldsymbol{v}}_E$ are constant on $a/v_{\mathrm{th},e}$ time scales, and so appear as additional 'equilibrium' terms in the short-wavelength electron gyrokinetic equation. By inspecting (2.2) we see that we are able to ascribe simple physical interpretations to the cross-scale terms: the term $\bar{\boldsymbol{v}}_E\cdot\boldsymbol{\nabla}\tilde{g}$ represents an advection term that will introduce velocity shear; and the gradient $\boldsymbol{\nabla}\bar{g}$ appears in the term $\tilde{\boldsymbol{v}}_E\cdot(\boldsymbol{\nabla}F_0+\boldsymbol{\nabla}\bar{g})$, i.e. $\boldsymbol{\nabla}\bar{g}$ modifies the usual equilibrium drive of instability $\boldsymbol{\nabla}F_0$. Equations (2.2) and (2.3) are solved in a thin ES flux tube embedded within a larger IS flux tube, see figure 1 for an illustration. In each ES flux tube, $\boldsymbol{\nabla}\bar{g}$ and $\bar{\boldsymbol{v}}_E$ take values that are constant in the perpendicular-to-the-field plane; the effects of the perpendicular derivatives of $\boldsymbol{\nabla}\bar{g}$ and $\bar{\boldsymbol{v}}_E$ are small by $(m_e/m_i)^{1/2}$ and so only appear at higher order. However, both $\boldsymbol{\nabla}\bar{g}$ and $\bar{\boldsymbol{v}}_E$ can vary along the field line: this results in a background drive of instability that is no longer uniform in θ, and in suppression of short-wavelength instabilities due to parallel-to-the-field $\boldsymbol{E}\times\boldsymbol{B}$ shearing by long-wavelength flows. The component of $\bar{\boldsymbol{v}}_E$ due to the piece of the electrostatic potential $\bar{\phi}$ that is constant on the flux surface may be removed from (2.2) by boosting to a toroidally rotating frame (Hardman 2019); this component of $\bar{\boldsymbol{v}}_E$ can only change the instability frequency by a Doppler shift. We discuss the physical interpretation of these cross-scale interaction mechanisms further in § 4.

To enable the study of cross-scale interaction in this multiscale framework, the cross-scale terms $\bar{\boldsymbol{v}}_E\cdot\boldsymbol{\nabla}\tilde{g}$ and $\tilde{\boldsymbol{v}}_E\cdot\boldsymbol{\nabla}\bar{g}$ in (2.2) were implemented in the δf gyrokinetic code GS2 (Kotschenreuther, Rewoldt & Tang 1995; Hardman 2019).

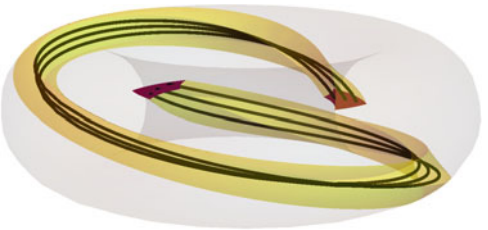

FIGURE 1. Illustration of a large-scale, IS flux tube with several narrow ES flux tubes embedded within it.

3. Numerical results

In this paper, we address the key question of how the linear stability of the ETG mode is affected by cross-scale interaction. We focus on a plasma in which single-scale microturbulence is well understood: we use a simple magnetic geometry consisting of concentric circular flux surfaces, with parameters largely corresponding to the widely used Cyclone Base Case benchmark (CBC) (Dimits *et al.* 2000). In the simulations we take a to be the half-diameter of the last closed flux surface; we take the normalised minor radius at the centre of the flux tube $\rho_0 = r_0/a = 0.54$, with r_0 the minor radius of the flux surface; the major radius $R = 3.0a$; the safety factor at the centre of the flux tube $q_0 = 1.4$; the magnetic shear $\hat{s} = \rho\,\mathrm{d}\ln q/\mathrm{d}\rho = 0.8$; equal ion and electron temperatures $T_i = T_e = T$; the normalised temperature gradient $a/L_T = -\mathrm{d}\ln T/\mathrm{d}\rho = 2.3$; the normalised density gradient $a/L_n = -\mathrm{d}\ln n/\mathrm{d}\rho = 0.733$; the normalised self-collision frequencies $a\nu_{\mathrm{ii}}/v_{\mathrm{th},i} = a\nu_{\mathrm{ee}}/v_{\mathrm{th},e} = 10^{-2}$; and the electron-to-deuterium-ion mass ratio $m_e/m_i = 2.7\times10^{-4} \approx 1/3670$. In the IS simulations, instead of explicitly implementing the parallel-orbit-averaged equation for the electron species, we impose that the passing, non-zonal electron response is Boltzmann, whilst continuing to solve for the remainder of the electron distribution function with the usual GS2 algorithm. In the limit that $(m_e/m_i)^{1/2} \to 0$, this has the effect of solving the electron parallel-orbit-averaged equation numerically. The GS2 algorithm employs (ε, λ) velocity coordinates, and retains the bounce points in θ for all particles: in this scheme, particles with large parallel velocities have a response that is an orbit average over the fluctuations. To verify that $m_e/m_i = 2.7\times10^{-4}$ is sufficiently small for the IS turbulence here to be in the $(m_e/m_i)^{1/2} \to 0$ limit, we performed additional IS simulations with $m_e/m_i = 2.7\times10^{-12}$ and a Boltzmann passing, non-zonal electron response. Identical IS fluxes and cross-scale interactions with ETG instabilities were found at $m_e/m_i = 2.7\times10^{-12}$ and $m_e/m_i = 2.7\times10^{-4}$. Physically, this is because the electron bounce time is shorter than the correlation time of the IS turbulence considered here.

To assess the impact of cross-scale interaction on the ETG instability we carry out the following numerical investigation. We perform simulations of long-wavelength ITG-driven turbulence, using the resolutions detailed in appendix A.1. We compute a sample of $\nabla\bar{g}(\theta, \varepsilon, \lambda, \sigma)$ and $\bar{\boldsymbol{v}}_E(\theta)$ at 6 times t_s, on a 6×5 grid in radial and binormal position, x_s and y_s, respectively. For each t_s at every sampled (x_s, y_s) we compute the ETG linear growth rate $\gamma(t_s, x_s, y_s)$, including the cross-scale interaction terms $\bar{\boldsymbol{v}}_E\cdot\nabla\tilde{g}$ and $\tilde{\boldsymbol{v}}_E\cdot\nabla\bar{g}$ in (2.2). The resolutions used for the linear calculations are detailed in appendix A.2. This statistical approach is necessary because $\bar{\boldsymbol{v}}_E$ and $\nabla\bar{g}$ must be calculated from turbulent fields which may vary intermittently in time and space. Figure 2(*a*) shows the spatially averaged IS potential $\langle\bar{\phi}^2\rangle_{x,y,\theta}(t)$, with sampled times indicated with a vertical line; and figure 2(*b*) shows the IS potential $\bar{\phi}(x, y)$ at the outboard midplane

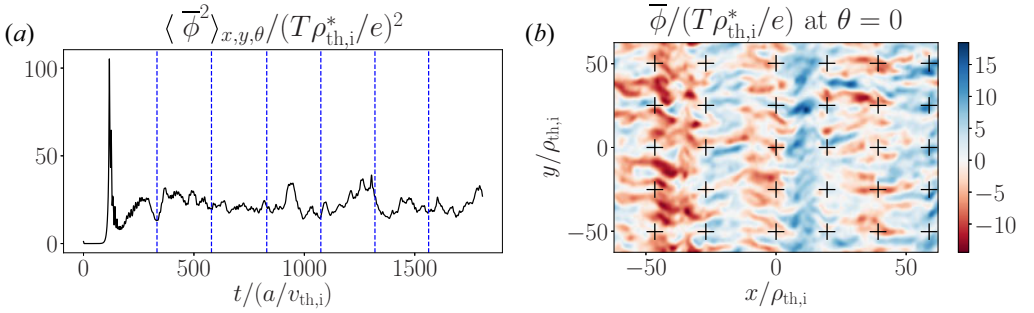

FIGURE 2. (*a*) The IS potential $\bar{\phi}$ in units of $\rho^*_{\mathrm{th},i} = \rho_{\mathrm{th},i}/a$, shown as a function of time (volume-averaged), and (*b*) at the outboard midplane at $t \simeq 1560a/v_{\mathrm{th},i}$. Times at which the IS turbulence is sampled are indicated with vertical lines, and sampled (x_s, y_s) positions are indicated by crosses.

at time $t \simeq 1560a/v_{\mathrm{th},i}$ (the last sampled time in figure 2*a*), with sampled positions indicated with crosses. The (x, y) coordinates are proportional to the flux-surface and field-line labels, ψ and α, respectively, that define the magnetic field $\boldsymbol{B} = \nabla\alpha \times \nabla\psi$: we use the perpendicular-to-the-field coordinates (x, y) that are defined to have units of length, i.e. $x = (\psi - \psi_0)(\mathrm{d}\psi/\mathrm{d}x)^{-1}$ and $y = (\alpha - \alpha_0)(\mathrm{d}\alpha/\mathrm{d}y)^{-1}$, respectively, with (ψ_0, α_0) the coordinates of the centre of the IS flux tube, $\mathrm{d}\psi/\mathrm{d}x = B_{\mathrm{ref}} a\rho_0/q_0$ and $\mathrm{d}\alpha/\mathrm{d}y = B_{\mathrm{ref}} a\partial\rho/\partial\psi|_{\rho_0}$, where B_{ref} is a reference magnetic field. We take B_{ref} to be the toroidal magnetic field strength on the flux surface ψ_0 at the major radius $R_{\mathrm{ref}} = (R_{\mathrm{max}} + R_{\mathrm{min}})/2$, where R_{max} and R_{min} are the maximum and minimum major radial positions taken in the flux tube, respectively. We note that we choose to define the poloidal angle θ in the simulations to be such that $\boldsymbol{b} \cdot \nabla\theta$ is constant in θ.

Figure 3 shows the linear growth rate γ spectrum in the absence of cross-scale interaction. In figure 3(*a*) we show $\gamma(k_y)$ for modes with $\hat{\theta}_0 = 0$, where $\hat{\theta}_0$ is the poloidal angle at which the wave fronts of the mode align with the minor radial direction of the flux surface. Modes with $\hat{\theta}_0 = 0$ have radially aligned wave fronts at the outboard midplane. Figure 3(*a*) shows that for the simulation parameters used in this paper, see curve (i), there is a natural stable gap in binormal wave number k_y between the ITG and ETG modes: this serves to define the cut-off between the IS and ES. We note that this separation of scales can become larger when both the drives of instability a/L_{T_i} and a/L_{T_e} are reduced, see curve (ii), whereas the separation can disappear for sufficiently strong drive or low collisionality, see, e.g., curve (iii). Collisional dissipation creates a stable gap in k_y between the ITG and the ETG modes through the following effects. First, collisional dissipation stabilises both the weakly growing ETG modes with $k_y\rho_{\mathrm{th},e} \ll 1$, and the ITG modes with $k_y\rho_{\mathrm{th},i} \gtrsim 1$. Second, collisions have the effect of detrapping trapped electrons with an enhanced collision frequency $\nu_{\mathrm{ee}}^{\mathrm{detrap}} \sim \nu_{\mathrm{ee}}/\epsilon$, where $\epsilon = r_0/R$ is the inverse aspect ratio. When the mode frequency ω is sufficiently small, i.e. $\omega/\nu_{\mathrm{ee}}^{\mathrm{detrap}} \lesssim 1$, the trapped electron drive of trapped electron modes (TEMs) (Adam, Tang & Rutherford 1976) and ITG modes is reduced, and hence TEMs and ITG modes that lie in the range $k_y\rho_{\mathrm{th},i} \gtrsim 1$ are stabilised, cf. Roach *et al.* (2009). In figure 3(*b*) we plot the full ETG linear growth rate spectrum $\gamma(k_y, \hat{\theta}_0)$ in the absence of cross-scale interaction. Note that the most unstable modes occur at $\hat{\theta}_0 = 0$. The dashed curve in figure 3(*b*) indicates the stability boundary where $\gamma = 0$, calculated with an interpolated spline fit. Figures 4(*a*) and 4(*b*) show the ETG growth rates in the presence of cross-scale interactions at two of the sampled IS positions

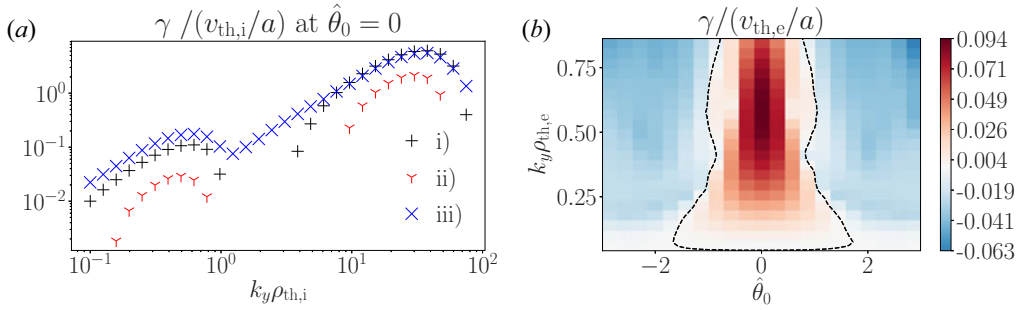

FIGURE 3. (*a*) The linear growth rate without cross-scale effects for three cases: (i) for the parameters given at the start of § 3 ($a/L_{T_i} = a/L_{T_e} = 2.3$ and $a\nu_{pp}/v_{\mathrm{th},p} = 10^{-2}$); (ii) for the case of reduced drive, with $a/L_{T_i} = a/L_{T_e} = 1.38$, holding $a\nu_{pp}/v_{\mathrm{th},p} = 10^{-2}$; and (iii) for the case of reduced collision frequency, with $a/L_{T_i} = a/L_{T_e} = 2.3$ and $a\nu_{pp}/v_{\mathrm{th},p} = 10^{-4}$. (*b*) The ETG growth rate in the absence of cross-scale interaction for the parameters given at the start of § 3 ($a/L_{T_e} = 2.3$ and $a\nu_{\mathrm{ee}}/v_{\mathrm{th},e} = 10^{-2}$). Modes within the dashed curve are unstable.

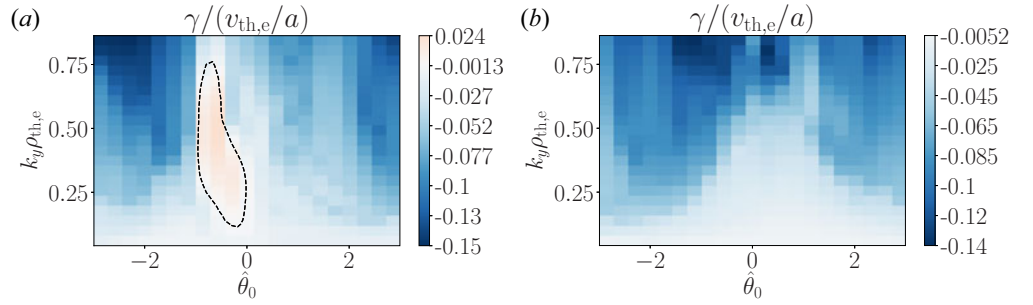

FIGURE 4. The ETG growth rate in the presence of cross-scale interaction due to IS turbulence: (*a*,*b*) show growth rates calculated at different (x_s, y_s) and times t_s. Note the suppression of the growth rate in (*a*,*b*) compared with figure 3(*b*).

and times. Comparing figure 3(*b*) with figures 4(*a*) and 4(*b*) shows that the effect of cross-scale interaction can be dramatic: in these examples the ETG mode is largely suppressed, and completely stabilised, respectively.

To determine the average, or typical effect of IS turbulence on the ETG instability we calculate the maximum ETG growth rate $\gamma_{\max}$ at every (t_s, x_s, y_s), where we note that the maximum γ may occur at a $(k_y, \hat{\theta}_0)$ that is different from the single-scale case. Figure 5(*a*) shows that the majority of IS drifts and gradients had the effect of stabilising the ETG mode: we find that $\gamma_{\max} < 0$ at 115 (t_s, x_s, y_s) within the sample of 180, with only a single (t_s, x_s, y_s) showing a $\gamma_{\max}$ larger than the maximum growth rate in the absence of cross-scale interaction. This is illustrated further in figure 5(*b*), which shows that the average of the sampled ETG growth rates $\langle\gamma\rangle_{t_s,x_s,y_s}$ is negative, for all $(k_y, \hat{\theta}_0)$. In figure 6 we show the distributions of k_y and $\hat{\theta}_0$ for the fastest-growing ETG modes in the presence of IS turbulence, with only modes that have $\gamma_{\max} > 0$ included in the histograms. Note the significant spread in k_y and $\hat{\theta}_0$ that results from the cross-scale interactions with the IS turbulence.

These results indicate that strongly driven ITG turbulence can suppress, or stabilise, strongly driven ETG instabilities. This is in agreement with results from multiscale DNS

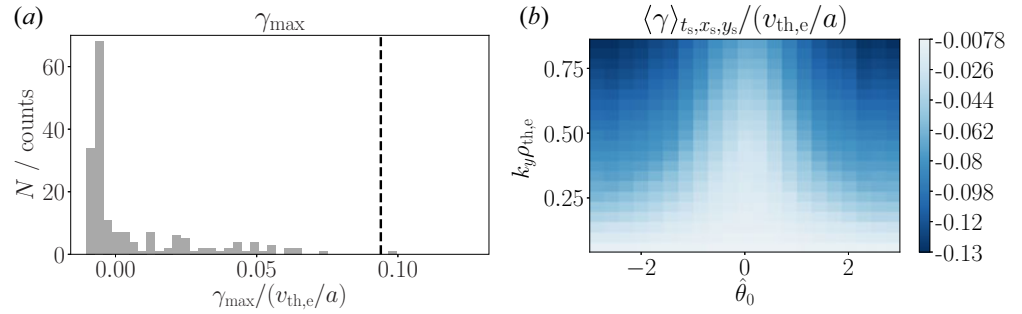

FIGURE 5. (*a*) The maximum ETG growth rate $\gamma_{\max}$ computed including the cross-scale terms $\bar{\boldsymbol{v}}_E \cdot \boldsymbol{\nabla}\tilde{g}$ and $\tilde{\boldsymbol{v}}_E \cdot \boldsymbol{\nabla}\bar{g}$ in (2.2). We see that the typical effect of cross-scale interaction for these parameters is to stabilise the ETG mode. The dashed vertical line indicates the value of $\gamma_{\max}$ for the ETG mode in the absence of cross-scale interaction. (*b*) The average ETG growth rate $\langle\gamma\rangle_{t_s,x_s,y_s}$ as a function of $(k_y, \hat{\theta}_0)$.

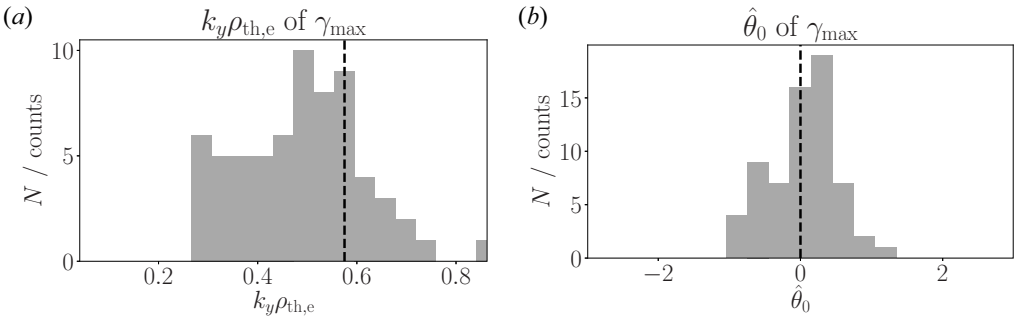

FIGURE 6. (*a*) The k_y of the fastest-growing ETG mode. (b) The $\hat{\theta}_0$ of the fastest-growing ETG mode. The dashed lines indicate the k_y and $\hat{\theta}_0$ of the ETG mode in the absence of IS turbulence. Only modes with $\gamma_{\max} > 0$ are included in the figures.

which show reduced short-wavelength heat transport in the presence of strongly driven ITG instabilities, see, e.g., Howard *et al.* (2016*a*,*b*) and Maeyama *et al.* (2015). In the following sections we explore the physical mechanisms that result in the stabilisation of the ETG instability in the $(m_e/m_i)^{1/2} \to 0$ limit.

4. Physical mechanisms and interpretation

The cross-scale terms in (2.2), $\tilde{\boldsymbol{v}}_E \cdot \boldsymbol{\nabla}\bar{g}$ and $\bar{\boldsymbol{v}}_E \cdot \boldsymbol{\nabla}\tilde{g}$, have intuitive physical interpretations. The gradient $\boldsymbol{\nabla}\bar{g}$ modifies the local gradients of the background Maxwellian distribution function $\boldsymbol{\nabla}F_0$, and thus modifies the instability drive. The drift $\bar{\boldsymbol{v}}_E$ is a cross-field flow that advects ES fluctuations and that can vary strongly in the parallel-to-the-field direction. This parallel-to-the-field variation introduces a new parallel length scale and means that $\bar{\boldsymbol{v}}_E$ cannot simply be removed from the equations by changing to a rotating or boosted frame. The most unstable toroidal instabilities typically have a parallel wave number $k_\parallel$ that is set by the connection length qR, i.e. $k_\parallel qR \sim 1$, cf. Parisi *et al.* (2020). Parallel-to-the-field shearing of the ETG fluctuations acts to increase $k_\parallel$ by imposing a parallel length scale such that $k_\parallel qR \gtrsim 1$, and hence stabilises toroidal modes. We illustrate the physical picture for parallel-to-the-field shearing in figure 7. Figure 7(*a*) depicts the field-aligned structure of the toroidal ETG mode in the absence of

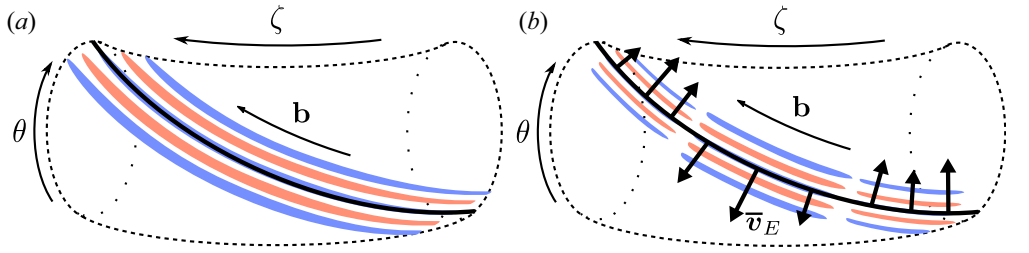

FIGURE 7. (*a*) Cartoon of field-aligned contours of ETG-driven potential fluctuations in the absence of parallel-to-the-field shear. (*b*) The same ETG-driven mode in the presence of an $\boldsymbol{E} \times \boldsymbol{B}$ drift that varies in the direction of $\boldsymbol{b}$ on a scale shorter than the connection length by a factor of order unity: the parallel-to-the-field scale of the mode is shortened.

parallel shearing. Figure 7(*b*) shows the result of imposing a cross-field flow that varies along the magnetic field line: the $k_\parallel$ of the ETG mode is now set by the parallel-to-the-field structure of $\bar{\boldsymbol{v}}_E$, and not by the connection length qR. The drift $\bar{\boldsymbol{v}}_E$ varies strongly in the direction of $\boldsymbol{b}$ because at a specific x_s and y_s the IS potential $\bar{\phi} = \bar{\phi}(\theta)$. We note that we may express $\nabla\bar{g} = \nabla\bar{h} + \nabla(e\bar{\phi}/T_e)F_0$, with $\bar{h}$ the non-adiabatic response of electrons at IS. In the orbit-averaged model $\bar{h}$ is a constant in θ, at fixed (ε, λ), and is zero in the passing piece of the velocity space for modes which oscillate in y (non-zonal modes) (Hardman *et al.* 2019). Despite this, $\bar{g}$ can vary strongly in the direction of $\boldsymbol{b}$ because of the contribution from the adiabatic response $e\bar{\phi}F_0/T_e$. Hence, $\nabla\bar{g}$ contains a contribution to the density gradient $\nabla(e\bar{\phi}/T_e)F_0$ that has the effect that the total modified drive of instability $\nabla\bar{g} + \nabla F_0$ drives the mode non-uniformly in θ: this effect can also impose an increased $k_\parallel$ on the mode. We note that the contribution to $\nabla\bar{g}$ from the non-adiabatic electron response $\nabla\bar{h}$ contains modifications to the background density and temperature gradients, and gradients of higher-order velocity moments that may drive or suppress instabilities. It is worth noting that the velocity moments of $\bar{h}$ do, in general, depend on θ: this is a consequence of the fact that trapped particles can only access a limited range of θ, and the fact that the non-zonal, passing electron non-adiabatic response vanishes in the orbit-averaged model.

To shed light on the physical mechanisms underlying the result shown in figure 5, we separately consider the effect of including $\nabla\bar{g}$ and $\bar{\boldsymbol{v}}_E$. In figure 8(*a*) we show the histogram of the maximum ETG growth rate $\gamma_{\max}$ computed including only the cross-scale term $\bar{\boldsymbol{v}}_E \cdot \nabla\tilde{g}$ (setting $\nabla\bar{g} = 0$). In figure 8(*b*) we show the histogram of $\gamma_{\max}$ computed including only the cross-scale term $\tilde{\boldsymbol{v}}_E \cdot \nabla\bar{g}$ (setting $\bar{\boldsymbol{v}}_E = 0$). We see by comparing figures 5(*a*), 8(*a*) and 8(*b*) that both the effect of parallel-to-the-field shearing and modifications to the background gradients are important in the ETG stabilisation shown in figure 5. From figure 8(*a*) we see that the effect of $\bar{\boldsymbol{v}}_E$ appears to be uniformly stabilising, i.e. there are no instances where $\gamma_{\max}$ becomes larger than the single-scale ETG growth rate. However, in figure 8(*b*) we see that the effect of $\nabla\bar{g}$ almost always stabilises the ETG mode, but in rare instances can make the ETG mode more unstable. In the following sections we study these cross-scale physics mechanisms in more detail and provide qualitative explanations for these results.

We note that our decomposition of the cross-scale terms, while physically motivated, is not unique. In particular, we recall that we can further decompose $\nabla\bar{g} = \nabla\bar{h} + \nabla(e\bar{\phi}/T_e)F_0$. In figures 8(*c*) and 8(*d*) we show the cross-scale effects of $\nabla\bar{h}$ and $\nabla(e\bar{\phi}/T_e)F_0$ on the ETG mode separately. The piece due to the non-adiabatic response $\nabla\bar{h}$ can both drive and suppress the ETG mode, whereas the piece due to the adiabatic

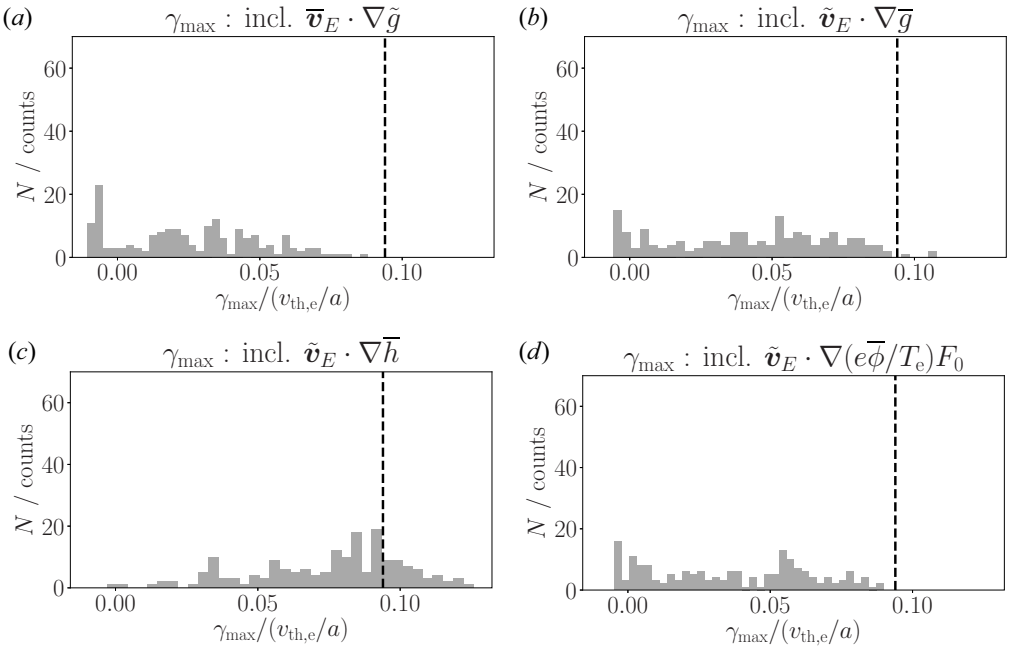

FIGURE 8. Histograms of the maximum ETG growth rate $\gamma_{\max}$ computed using (2.2), but including only the cross-scale terms indicated. The dashed vertical line indicates the maximum ETG growth rate in the absence of cross-scale coupling.

response $\nabla(e\bar{\phi}/T_e)F_0$ appears to only suppress the ETG mode. We give a qualitative explanation for this observation in § 6.

5. Evidence for parallel-to-the-field shearing

In this section we show that the physical picture given in figure 7 is consistent with the simulation results presented in § 3: the IS turbulence indeed shortens the parallel-to-the-field scale of the ETG modes. To demonstrate this we first consider the structure of the cross-scale terms and the structure of the ETG eigenmode in the ballooning coordinate, labelled by θ. The fastest-growing ETG mode from a single-scale simulation with CBC parameters occurs at $k_y\rho_{\mathrm{th},e} = 0.58$ and $\hat{\theta}_0 = 0$. Figure 9(*a*) compares the potential eigenmode for the $k_y\rho_{\mathrm{th},e} = 0.58$ and $\hat{\theta}_0 = 0$ mode from a single-scale simulation, to the $k_y\rho_{\mathrm{th},e} = 0.58$ and $\hat{\theta}_0 = 0$ mode obtained at a specific example space–time location in the IS turbulence. We see that the cross-scale interaction introduces oscillatory features into the potential eigenmode. This is a result of the variation of $\bar{\boldsymbol{v}}_E$ and $\nabla\bar{g} = \nabla(e\bar{\phi}/T_e)F_0 + \nabla\bar{h}$ along the magnetic field line. To illustrate this, in figure 9(*b*) we show the imposed IS $\boldsymbol{E}\times\boldsymbol{B}$ drift frequency

$$\bar{\omega}_{E\times B} = \frac{c\kappa_\rho}{B_{\mathrm{ref}}}\left(k_x\frac{\partial\bar{\phi}}{\partial y} - k_y\frac{\partial\bar{\phi}}{\partial x}\right), \tag{5.1}$$

with k_x the field-aligned radial wave number of the ETG mode, i.e. the wavenumber $\boldsymbol{k} = k_x\nabla x + k_y\nabla y$, and the geometrical factor $\kappa_\rho = B_{\mathrm{ref}}(\mathrm{d}x/\mathrm{d}\psi)(\mathrm{d}y/\mathrm{d}\alpha) \simeq 1.01$ for CBC parameters. The frequency $\bar{\omega}_{E\times B}$ is compared with the thermal magnetic

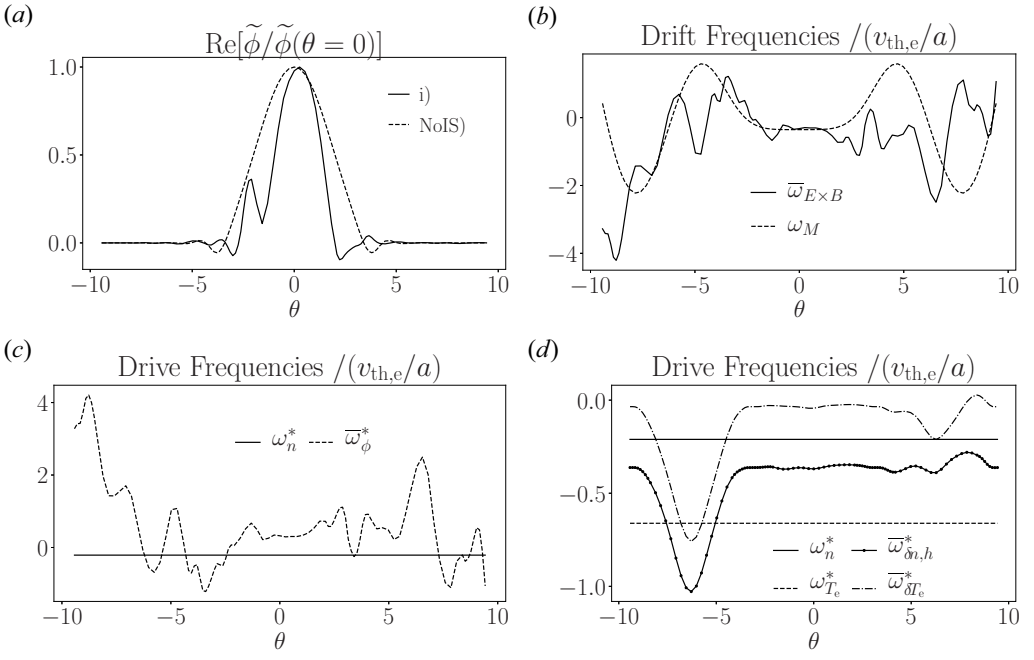

FIGURE 9. (*a*) The real part of the normalised potential eigenmode for the fastest-growing ETG mode for (i) a specific instance of IS gradients and NoIS) the eigenmode in the absence of cross-scale coupling. The normalised growth rates are $\gamma/(v_{\mathrm{th},e}/a) = 0.045$ and 0.094, respectively. For simplicity, we chose to compare a case where the fastest-growing mode in the presence of IS turbulence appears at $k_y\rho_{\mathrm{th},e} = 0.58$ and $\hat{\theta}_0 = 0.0$. (*b*) The thermal magnetic drift frequency ω_M compared to the IS $\boldsymbol{E}\times\boldsymbol{B}$ drift frequency $\bar{\omega}_{E\times B}$. (*c*) The drive frequencies due to equilibrium density gradients ω_n^*, and due to gradients in the adiabatic part of the IS electron distribution function $\bar{\omega}_\phi^*$. (*d*) The drive frequencies due to equilibrium temperature gradients $\omega_{T_e}^*$, and gradients of temperature and density in the non-adiabatic part of the IS electron distribution function, $\bar{\omega}_{\delta T_e}^*$ and $\bar{\omega}_{\delta n,h}^*$, respectively.

drift frequency

$$\omega_M = \frac{v_{\mathrm{th},e}^2}{\Omega_e}\boldsymbol{k}\cdot\boldsymbol{b}\times\left(\frac{\nabla B}{B} + \boldsymbol{b}\cdot\nabla\boldsymbol{b}\right). \tag{5.2}$$

In figure 9(*c*) we show the drive frequencies associated with the $\nabla(e\bar{\phi}/T_e)F_0$ piece of $\nabla\bar{g}$, $\bar{\omega}_\phi^* = -\bar{\omega}_{E\times B}$, compared with the background density gradient drive $\omega_n^* = -ck_yT_e/eB_{\mathrm{ref}}L_n$; and in figure 9(*d*) we show the background temperature gradient drive frequency $\omega_{T_e}^* = -ck_yT_e/eB_{\mathrm{ref}}L_{T_e}$, and the drive frequencies due to the gradients in the density $\overline{\delta n_h}$ and temperature $\overline{\delta T_e}$ moments of $\nabla\bar{h}$,

$$\bar{\omega}_{\delta n,h}^* = \frac{c\kappa_\rho T_e}{eB_{\mathrm{ref}}}\left(\frac{k_y}{n}\frac{\partial\overline{\delta n_h}}{\partial x} - \frac{k_x}{n}\frac{\partial\overline{\delta n_h}}{\partial y}\right) \tag{5.3}$$

and

$$\bar{\omega}_{\delta T_e}^* = \frac{c\kappa_\rho T_e}{eB_{\mathrm{ref}}}\left(\frac{k_y}{T_e}\frac{\partial\overline{\delta T_e}}{\partial x} - \frac{k_x}{T_e}\frac{\partial\overline{\delta T_e}}{\partial y}\right), \tag{5.4}$$

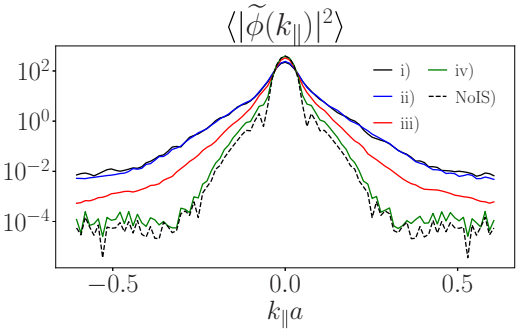

FIGURE 10. A comparison of the power spectrum of the electrostatic potential $\tilde{\phi}$ of the fastest-growing ETG ballooning mode as a function of $k_\parallel$ for several cases. In case NoIS) we show the power spectrum of the fastest-growing ballooning mode in the absence of cross-scale coupling. The remaining curves show the (t_s, x_s, y_s)-averaged power spectrum of the fastest-growing ETG mode in the case that: (i) both cross-scale terms $\bar{\boldsymbol{v}}_E \cdot \boldsymbol{\nabla}\tilde{g}$ and $\tilde{\boldsymbol{v}}_E \cdot \boldsymbol{\nabla}\bar{g}$ are included; (ii) only the shearing term $\bar{\boldsymbol{v}}_E \cdot \boldsymbol{\nabla}\tilde{g}$ is included; (iii) only the modification to $\boldsymbol{\nabla}F_0$ from the adiabatic response of electrons is included, i.e. $\tilde{\boldsymbol{v}}_E \cdot \boldsymbol{\nabla}(e\bar{\phi}/T_e)F_0$; and (iv) only the modification to $\boldsymbol{\nabla}F_0$ from the non-adiabatic response of electrons is included, i.e. $\tilde{\boldsymbol{v}}_E \cdot \boldsymbol{\nabla}\bar{h}$. To measure the spread of the distribution of $k_\parallel$ we use $\sigma_{k_\parallel}$, defined in (5.6). We find (i) $\sigma_{k_\parallel} = 0.065$, (ii) $\sigma_{k_\parallel} = 0.064$, (iii) $\sigma_{k_\parallel} = 0.043$, (iv) $\sigma_{k_\parallel} = 0.031$ and (NoIS) $\sigma_{k_\parallel} = 0.027$.

respectively. There are two key feature to note in figures 9(*b*), 9(*c*) and 9(*d*). First, the frequencies that mediate the effects of IS turbulence on ETG modes are comparable in amplitude with the equilibrium drive and thermal magnetic frequencies. Second, the frequencies vary in θ on the scale of the ETG eigenmode in 9(*a*). In the strongly driven turbulence that we consider here, we have found that the θ dependence of $\bar{\omega}_{E\times B}$ cannot be described by a simple function with few parameters. In consequence, simplified quantitative modelling of the effects of parallel-to-the-field shearing by $\bar{\boldsymbol{v}}_E$ is challenging. As we discuss in § 6, we find that it is possible to approximate $\bar{\omega}^*_{\delta n,h}$ and $\bar{\omega}^*_{\delta T_e}$ by a constant value.

To assess whether or not the physical picture in figure 7 is consistent with the simulation results, we calculate the $k_\parallel$ spectrum of the fastest-growing ETG mode at each (t_s, x_s, y_s) in the sample. For a single ballooning mode, we define the $k_\parallel$ spectrum to be $|\tilde{\phi}(k_\parallel)|^2$, where

$$\tilde{\phi}(k_\parallel) = \int_{-\infty}^{\infty} \exp[\mathrm{i}k_\parallel z]\tilde{\phi}(z)\,\mathrm{d}z, \tag{5.5}$$

cf. Parisi *et al.* (2020), with $z = \theta/\boldsymbol{b}\cdot\boldsymbol{\nabla}\theta$, and $\tilde{\phi}(z)$ is normalised so that the maximum value of $\tilde{\phi}(z)$ is 1: this maximum may occur away from $z = 0$. We note that we define the θ coordinate in the simulations such that $\boldsymbol{b}\cdot\boldsymbol{\nabla}\theta$ is constant in θ. In figure 10 we compare $|\tilde{\phi}(k_\parallel)|^2$ for the fastest-growing ETG mode in the absence of cross-scale interaction with the average $k_\parallel$ spectrum $\langle|\tilde{\phi}(k_\parallel)|^2\rangle$ of the fastest-growing ETG modes in several calculations including various combinations of the cross-scale interaction terms. Figure 10 indicates that cross-scale interaction introduces tails in the $k_\parallel$ spectra. These tails correspond to the oscillatory structure of the eigenmode shown in figure 9(*a*). To quantify the size of these tails, we introduce a measure of the spread of the distribution of $k_\parallel$:

$$\frac{\sigma^2_{k_\parallel}}{2} = \frac{\int k_\parallel^2\langle|\tilde{\phi}(k_\parallel)|^2\rangle\,\mathrm{d}k_\parallel}{\int\langle|\tilde{\phi}(k_\parallel)|^2\rangle\,\mathrm{d}k_\parallel}. \tag{5.6}$$

For the fastest-growing ETG mode in the absence of cross-scale interaction $\sigma_{k_\parallel} = 0.027$. For the average $k_\parallel$ spectrum of the fastest-growing ETG modes in the presence of all cross-scale interaction terms we find that $\sigma_{k_\parallel} = 0.065$. This indicates that the effect of cross-scale interaction is indeed to introduce larger $k_\parallel$ into the ETG mode. Figure 10 indicates that the dominant component of the $k_\parallel$ tails is introduced by the parallel shearing term $\bar{\boldsymbol{v}}_E \cdot \boldsymbol{\nabla}\tilde{g}$. We also note that the term $\tilde{\boldsymbol{v}}_E \cdot \boldsymbol{\nabla}\bar{h}$ introduces almost no $k_\parallel$ component: cross-scale interaction via $\tilde{\boldsymbol{v}}_E \cdot \boldsymbol{\nabla}\bar{h}$ leaves the form of the ETG eigenmode unchanged. This is consistent with the fact that $\bar{h}$ is constant in θ at fixed $(\varepsilon, \lambda, \sigma, x, y)$ in the parallel-orbit-averaged model.

6. Modifications to the drives of instability

The physical interpretation of the impact of $\boldsymbol{\nabla}\bar{g}$ in (2.2) is that $\boldsymbol{\nabla}\bar{g}$ modifies the background gradients in $\boldsymbol{\nabla}F_0$ that drive the instability. As discussed in § 4, $\boldsymbol{\nabla}\bar{g}$ is, in general, a complicated function of $(\theta, \varepsilon, \lambda)$. In this section we examine to what extent we can model $\boldsymbol{\nabla}\bar{g}$ by simple modifications to the values of a/L_{T_e} and a/L_n locally in the IS flux tube. For this we use the results of the simulations presented in figures 8(*b*), 8(*c*) and 8(*d*). This simplified model should be valid when the plasma is collisional and the fluctuations are zonally dominated: in this limit, $\bar{h}$ can be approximated as a perturbed Maxwellian that has no variation within a flux surface. We realise this limiting scenario in § 7.

We present the maximum ETG growth rate for the CBC magnetic geometry as a function of the background temperature and density gradients, $\gamma_{\max}^{\mathrm{CBC}}(a/L_{T_e}, a/L_n)$, in figure 11(*a*). We define effective background temperature and density gradients,

$$\frac{a}{L_{T_e}^{\mathrm{eff}}} = \frac{a}{L_{T_e}} - \left\langle \frac{a\kappa_\rho}{T_e} \frac{\partial \overline{\delta T_e}}{\partial x} \right\rangle_\theta , \tag{6.1}$$

$$\frac{a}{L_{n,h}^{\mathrm{eff}}} = \frac{a}{L_n} - \left\langle \frac{a\kappa_\rho}{n} \frac{\partial \overline{\delta n_h}}{\partial x} \right\rangle_\theta , \tag{6.2}$$

and

$$\frac{a}{L_n^{\mathrm{eff}}} = \frac{a}{L_n} - \left\langle \frac{a\kappa_\rho}{n} \frac{\partial \overline{\delta n}}{\partial x} \right\rangle_\theta , \tag{6.3}$$

respectively, with $\langle\cdot\rangle_\theta = \int_{-\pi}^{\pi} \cdot \, \mathrm{d}\theta / \boldsymbol{B} \cdot \boldsymbol{\nabla}\theta$ an average in θ between $(-\pi, \pi)$ at fixed (x, y), $\overline{\delta n_h}$ and $\overline{\delta T_e}$ the density and temperature moments of $\bar{h}$, respectively, and $\overline{\delta n} = \overline{\delta n_h} + ne\bar{\phi}/T_e$. The normalised density gradient scale $a/L_{n,h}^{\mathrm{eff}}$ measures the effective change to a/L_n by density gradients in the long-wavelength non-adiabatic response of electrons, whereas a/L_n^{eff} measures the effective change to a/L_n by gradients in the total long-wavelength density fluctuation.

In figure 11(*b*) we show that there is a strong correlation between the $\gamma_{\max}$ calculated using (2.2) including only the cross-scale term due to the IS, non-adiabatic electron response $\tilde{\boldsymbol{v}}_E \cdot \boldsymbol{\nabla}\bar{h}$ and the model growth rate $\gamma_{\max}^{\mathrm{CBC}}(a/L_{T_e}^{\mathrm{eff}}, a/L_{n,h}^{\mathrm{eff}})$. In contrast, in figure 11(*c*) we show that the cross-scale interaction due to $\boldsymbol{\nabla}\bar{g}$ cannot be modelled by $\gamma_{\max}^{\mathrm{CBC}}(a/L_{T_e}^{\mathrm{eff}}, a/L_n^{\mathrm{eff}})$. Instead, the model $\gamma_{\max}^{\mathrm{CBC}}$ almost always overestimates the growth rate of the ETG modes. We can understand these results by referring to figure 10. Cross-scale interaction due to the electron non-adiabatic response $\boldsymbol{\nabla}\bar{h}$ did not change the $k_\parallel$ spectrum of the ETG eigenmodes: $\boldsymbol{\nabla}\bar{h}$ has the effect of making the mode more or less unstable by

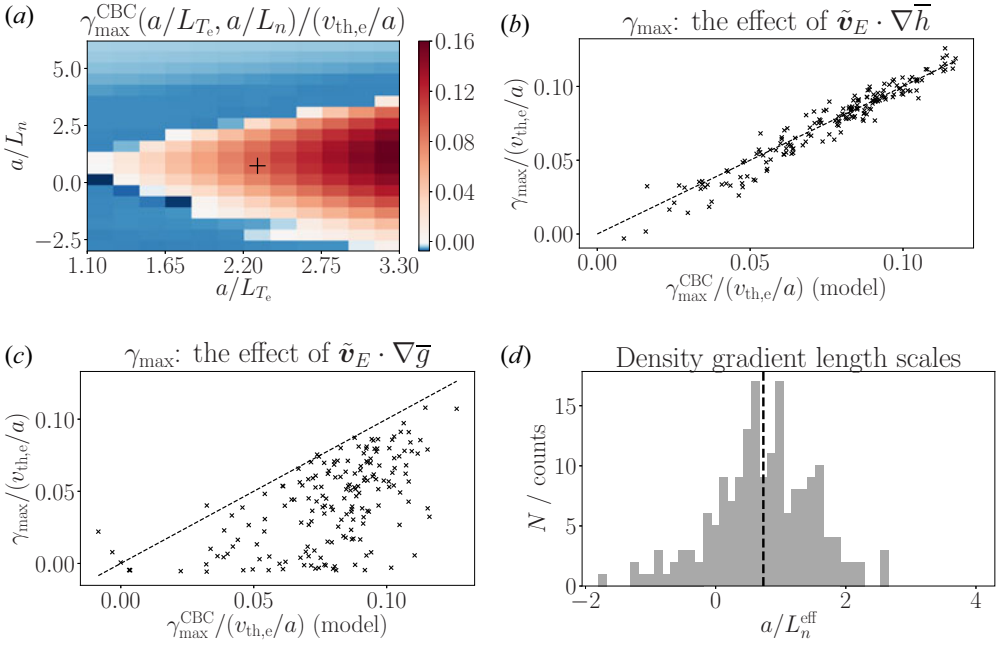

FIGURE 11. (*a*) The maximum ETG growth rate for CBC magnetic geometry $\gamma_{\max}^{\mathrm{CBC}}$ as a function of the normalised background gradient length scales a/L_{T_e} and a/L_n. The cross indicates the nominal CBC values of $a/L_{T_e} = 2.3$ and $a/L_n = 0.733$. (*b*) The maximum ETG growth rate $\gamma_{\max}$ including only the effects of the cross-scale term $\tilde{\boldsymbol{v}}_E \cdot \nabla\bar{h}$ compared with the model growth rate $\gamma_{\max}^{\mathrm{CBC}}(a/L_{T_e}^{\mathrm{eff}}, a/L_{n,h}^{\mathrm{eff}})$. The dashed line indicates the required slope for a perfect correlation. (*c*) $\gamma_{\max}$ including the effects of the cross-scale term $\tilde{\boldsymbol{v}}_E \cdot \nabla\bar{g}$ compared with the model growth rate $\gamma_{\max}^{\mathrm{CBC}}(a/L_{T_e}^{\mathrm{eff}}, a/L_n^{\mathrm{eff}})$. (*d*) The histogram of density gradient length scales a/L_n^{eff}. The dashed line indicates $a/L_n^{\mathrm{eff}} = 0.733$.

changing the drives only. In contrast the difference between $\nabla\bar{g}$ and $\nabla\bar{h}$, $\nabla(e\bar{\phi}/T_e)F_0$, had the effect of introducing larger $k_\parallel$ components into the mode, which cannot be captured by simple modifications to a/L_n and a/L_{T_e}. The fact that $\gamma_{\max}^{\mathrm{CBC}}(a/L_{T_e}^{\mathrm{eff}}, a/L_n^{\mathrm{eff}})$ typically overestimates the ETG growth rate in figure 11(*c*) indicates that the effect of the parallel-to-the-field variation in $\nabla(e\bar{\phi}/T_e)F_0$ is stabilising. These results suggest that in general we can characterise $\nabla\bar{g}$ as having two distinct components: first, a perturbed Maxwellian that simply shifts the equilibrium density and temperature gradients by constant values; and, second, a density gradient from the long-wavelength electron adiabatic response that varies in the parallel-to-the-field coordinate. Whilst the former component may in general stabilise or destabilise the ETG mode, the latter component almost always appears to be stabilising. The effect of $\nabla\bar{g}$ on an ETG mode depends on the relative importance of these two components.

Finally, we return to the result presented in figure 8(*b*): the average effect of $\nabla\bar{g}$ was to suppress ETG instability. We can now understand this result qualitatively. First, the parallel-to-the-field variation in the adiabatic response $\nabla(e\bar{\phi}/T_e)F_0$ suppressed the instability by increasing the $k_\parallel$ in the ETG mode. Second, note that for particular the CBC equilibrium we have chosen, a/L_n maximises the ETG growth rate at fixed a/L_{T_e}, as shown in figure 11(*a*): any modification to a/L_n will reduce the ETG growth rate $\gamma_{\max}$. The histogram of density gradient length scales a/L_n^{eff} shown in figure 11(*d*) indicates that

the typical modification to a/L_n is sufficient to reduce $\gamma_{\max}$ by an amount of order unity. This second stabilising effect is likely to be special to this equilibrium.

7. Cross-scale interaction in near-marginal turbulence

The simulation results presented in the previous sections were obtained for parameters where there is a strong background drive of instability for ITG modes at scales comparable with $\rho_{\mathrm{th},i}$ and ETG modes at scales comparable with $\rho_{\mathrm{th},e}$. In this section, we present results for the case where a/L_{T_i} and a/L_{T_e} are reduced so that both the ITG and ETG modes are driven near marginal stability. Weakly driven IS turbulence can reach a Dimits-shift regime where the fluxes are low, and a long-wavelength, long-lived zonal flow regulates the IS dynamics; see, e.g. , Dimits *et al.* (2000) and Rogers, Dorland & Kotschenreuther (2000). This represents a very different state from strongly driven, critically balanced, IS turbulence, cf. Barnes, Parra & Schekochihin (2011). Consequently, the relative importance of parallel-to-the-field shearing, parallel-to-the-field variation in the IS density gradient, and constant modifications to the background drives may differ in turbulence driven near marginal stability.

To obtain a near-marginal case, we use the parameters described in § 3, but reduce the normalised background temperature gradient length scales to $a/L_{T_e} = a/L_{T_i} = 1.38$. We use the resolutions given in appendix A.1, and we take $m_e/m_i = 2.7 \times 10^{-12}$ in the IS simulation. The IS turbulence is evolved until a long-lived, zonally dominated state emerges. We sample the IS gradients $\boldsymbol{\nabla}\bar{g}$ and drifts $\bar{\boldsymbol{v}}_E$ at radial coordinates in the IS flux tube x_s, for a single time t_s and binormal position y_s. In figure 12(*a*) we show $\bar{\phi}(x, y)$ at t_s for the near-marginal IS turbulence, with the sampled radial points taken along the dashed line. At each of the 128 equally spaced x_s positions we perform an ETG linear calculation, including the effects of cross-scale interaction via (2.2) and using resolutions detailed in appendix A.2. In contrast to the strongly driven case, in figure 12(*b*) we show that the maximum growth rate of the ETG mode $\gamma_{\max}$, calculated including both cross-scale interaction terms, $\bar{\boldsymbol{v}}_E \cdot \boldsymbol{\nabla}\tilde{g}$ and $\tilde{\boldsymbol{v}}_E \cdot \boldsymbol{\nabla}\bar{g}$, is strongly correlated with the model growth rate $\gamma^{\mathrm{CBC}}_{\max}(a/L^{\mathrm{eff}}_{T_e}, a/L^{\mathrm{eff}}_n)$, with the effective density gradient scales $a/L^{\mathrm{eff}}_{T_e}$ and a/L^{eff}_n defined in (6.1) and (6.3), respectively, and $\gamma^{\mathrm{CBC}}_{\max}$ shown in figure 11(*a*). The imperfections in the correlation in figure 12(*b*) are primarily due to parallel-to-the-field shearing from the term $\bar{\boldsymbol{v}}_E \cdot \boldsymbol{\nabla}\tilde{g}$ in (2.2) (cf. figure 10 which shows that $\bar{\boldsymbol{v}}_E \cdot \boldsymbol{\nabla}\tilde{g}$ injects larger $k_\parallel$ components than $\tilde{\boldsymbol{v}}_E \cdot \boldsymbol{\nabla}(e\bar{\phi}/T_e)F_0$). We infer that the effect of parallel-to-the-field shearing is weak in this near-marginal turbulence. We verified that the average $k_\parallel$ spectrum of the fastest-growing eigenmodes was identical in the cases with and without cross-scale interaction.

We can understand the result in figure 12(*b*) with the following intuition. The wavenumber spectrum of near-marginal turbulence is dominated by the zonal mode, a mode that is constant on each flux surface and only depends on the radial coordinate. As a consequence, perpendicular gradients in near-marginal turbulence are dominantly in the radial direction, and the variation of the electrostatic potential $\bar{\phi}$ in the parallel-to-the-field direction in the turbulence is weak. In this regime, the $\boldsymbol{E} \times \boldsymbol{B}$ advection term $\bar{\boldsymbol{v}}_E \cdot \boldsymbol{\nabla}\tilde{g}$ only modifies the ETG frequency by a Doppler shift (Hardman *et al.* 2019). Hence, the dominant cross-scale interaction term that alters the ETG growth rate is due to the radial gradients of the IS electron distribution function, i.e. $\boldsymbol{\nabla}\bar{g} \simeq \boldsymbol{\nabla}x\partial\bar{g}/\partial x$. In addition, if the plasma is sufficiently collisional then $\bar{g}$ is restricted to be a perturbed Maxwellian of only density and temperature gradients, and in consequence, the effect of cross-scale interaction in near-marginal turbulence may be parameterised with the effective background gradient length scales $a/L^{\mathrm{eff}}_{T_e}$ and a/L^{eff}_n. The results presented in this section demonstrate that this near-marginal cross-scale interaction regime can be realised.

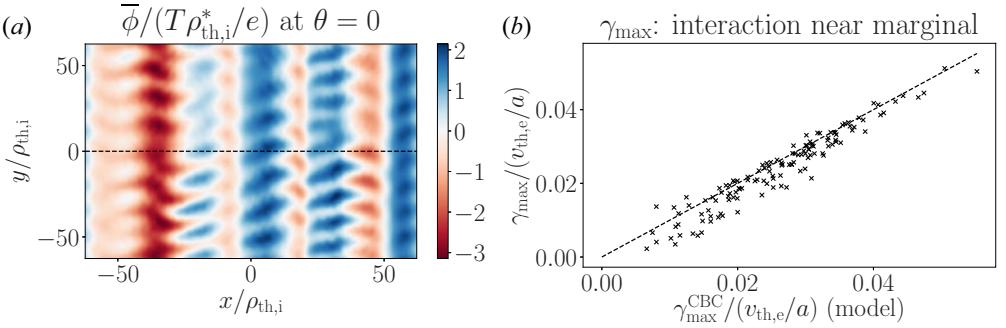

FIGURE 12. (a) Contours of the electrostatic potential $\bar{\phi}(x, y)$ for the sampled near-marginal IS turbulence. The 128 sampled positions x_s lie equally spaced on the dashed line. (b) The maximum ETG growth rate $\gamma_{\max}$ calculated using (2.2), including both cross-scale terms $\bar{\boldsymbol{v}}_E \cdot \boldsymbol{\nabla}\tilde{g}$ and $\tilde{\boldsymbol{v}}_E \cdot \boldsymbol{\nabla}\bar{g}$, compared with the model growth rate $\gamma^{\mathrm{CBC}}_{\max}(a/L^{\mathrm{eff}}_{T_e}, a/L^{\mathrm{eff}}_n)$ that is calculated using the results in figure 11(a) and definitions (6.1) and (6.3). The dashed line indicates the slope for a perfect correlation.

8. Discussion

The results presented in this paper were obtained in the limit $(m_e/m_i)^{1/2} \to 0$ with a theory that assumes scale-separation between long-wavelength and short-wavelength structures. This theory may not describe multiscale turbulence accurately for realistic values of $(m_e/m_i)^{1/2}$ under a variety of circumstances; e.g. when radially elongated ES structures (Dorland *et al.* 2000; Jenko *et al.* 2000; Jenko & Dorland 2002) grow to be as large as a typical IS eddy; or when there is no significant dissipation at wavelengths between the scales of the IS and ES turbulence. Nonetheless, in this paper we have demonstrated that significant cross-scale interactions do persist in the limit $(m_e/m_i)^{1/2} \to 0$: strongly driven, long-wavelength turbulence can stabilise a strongly driven ETG instability; and long-wavelength turbulence driven near marginal stability can change the growth rate of a weakly driven ETG mode by an order unity factor. The physical mechanisms responsible for these cross-scale interactions were shown to be, first, the parallel-to-the-field shearing of short-wavelength fluctuations by long-wavelength $\boldsymbol{E} \times \boldsymbol{B}$ drifts, and second, the modification of the background drives of instability by gradients in long-wavelength fluctuations. We demonstrated that the modification to the background drives could be characterised by two distinct pieces: a perturbed Maxwellian that affects a constant modification to the mean density gradient a/L_n and temperature gradient a/L_{T_e}; and a density gradient from the long-wavelength electron adiabatic response that varies in the parallel-to-the-field direction. In the case of strongly driven turbulence, the novel effects of both parallel-to-the-field $\boldsymbol{E} \times \boldsymbol{B}$ shearing and parallel-to-the-field variation in the long-wavelength density gradient were found to be stabilising. In the case of near-marginal turbulence, the effect of parallel-to-the-field $\boldsymbol{E} \times \boldsymbol{B}$ shearing was weak, parallel-to-the-field variation in the long-wavelength density gradient was unimportant, and the effect of cross-scale interaction could be parameterised solely with the effective background gradient length scales a/L^{eff}_n and $a/L^{\mathrm{eff}}_{T_e}$.

We can qualitatively explain the difference in the nature of the cross-scale interactions that we find in the cases of near-marginal and strongly driven turbulence. Near-marginal ITG turbulence is dominated by zonal modes, see, e.g. , Dimits *et al.* (2000) and Rogers *et al.* (2000). Zonal modes have a structure that depends only on radial position, and hence the long-wavelength $\boldsymbol{E} \times \boldsymbol{B}$ drift $\bar{\boldsymbol{v}}_E$ only has the effect of shifting the ETG fluctuation

frequency by a Doppler shift: for zonal modes where $\bar{\phi} = \bar{\phi}(x)$, the term $\bar{\boldsymbol{v}}_E \cdot \nabla \tilde{g}$ in (2.2) can be removed by boosting to a toroidally rotating frame (Hardman 2019). In this situation where the effect of parallel shearing is negligible, the dominant cross-scale interaction arises from the radial gradient $\nabla \bar{g} \simeq \nabla x \partial \bar{g}/\partial x$. If $\bar{g}$ is sufficiently close to a perturbed Maxwellian, perhaps as a result of moderate collisionality, then we find that $\partial \bar{g}/\partial x$ has dominant contributions from a density gradient and a temperature gradient. In contrast, strongly driven ITG turbulence is not zonally dominated, but consists of critically balanced turbulent eddies (Barnes *et al.* 2011) that can have a parallel correlation length as large as the device scale qR. Hence, $\nabla \bar{g}$ and $\bar{\boldsymbol{v}}_E$ can contain parallel-to-the-field variation that results in the non-uniform drive and the shearing apart of short-wavelength modes, respectively. In critically balanced turbulence, eddies with a greater k_y have a faster nonlinear turnover time, and hence a shorter parallel correlation length and a greater characteristic $k_\parallel \propto k_y^{4/3}(R/L_{T_i})^{4/3}$ (Barnes *et al.* 2011). A range of k_y modes in the inertial range can contribute to the gradient $\nabla \bar{g}$ and the drift $\bar{\boldsymbol{v}}_E$, with the result that $\nabla \bar{g}$ and $\bar{\boldsymbol{v}}_E$ can have parallel-to-the-field oscillations on scales shorter than qR. This observation leads us to expect that the impact of parallel-to-the-field shearing increases with increasing R/L_{T_i}.

A criterion for when to expect parallel-to-the-field $\boldsymbol{E} \times \boldsymbol{B}$ shear to suppress ETG modes can be obtained from a simple quasilinear argument. The effective shearing rate $\hat{\omega}_E$ should scale with the parallel-to-the-field variation in the cross-scale advection operator $\bar{\boldsymbol{v}}_E \cdot \nabla$, i.e. $\hat{\omega}_E \sim k_{\mathrm{ETG}} \partial \bar{\boldsymbol{v}}_E/\partial\theta$. We can expect parallel-to-the-field shear suppression when the effective shear rate

$$\hat{\omega}_E \gtrsim \gamma_{\mathrm{ETG}}; \tag{8.1}$$

i.e. when the shear rate is faster than the typical ETG mode growth rate γ_{ETG}, at a typical ETG mode wave number k_{ETG}. A quasilinear estimate gives $\bar{\boldsymbol{v}}_E \sim \gamma_{\mathrm{ITG}}/k_{\mathrm{ITG}}$, with γ_{ITG} and k_{ITG} the typical ITG mode growth rate and wave number, respectively. If we assume that the variation of $\bar{\boldsymbol{v}}_E$ in the parallel-to-the-field direction $\partial \bar{\boldsymbol{v}}_E/\partial\theta \sim \bar{\boldsymbol{v}}_E$, then we find that we can expect parallel-to-the-field shear suppression of ETG turbulence when

$$\frac{\gamma_{\mathrm{ITG}}}{k_{\mathrm{ITG}}} \gtrsim \frac{\gamma_{\mathrm{ETG}}}{k_{\mathrm{ETG}}}. \tag{8.2}$$

This result is consistent with observations of the behaviour of multiscale turbulence made in light of some DNS (Staebler *et al.* 2016, 2017; Creely *et al.* 2019), though their interpretation differs from that given here: Staebler *et al.* (2016, 2017) and Creely *et al.* (2019) neglect the variation of $\boldsymbol{E} \times \boldsymbol{B}$ drifts along field lines, and so neglect the key physical mechanism that is critical to the quasilinear argument: the effect of parallel-to-the-field $\boldsymbol{E} \times \boldsymbol{B}$ shear. We note that parallel-to-the-field flow shear has previously been considered as a part of a model of hyperviscous dissipation of ITG-driven turbulence (Smith 1997).

The suppression of short-wavelength turbulence seen in some DNS is often assumed to be the result of perpendicular-to-the-field $\boldsymbol{E} \times \boldsymbol{B}$ shearing by long-wavelength turbulence. In fact, that mechanism does not appear in the leading-order, scale-separated ES equation (2.2) (Hardman *et al.* 2019). In the limit that $(m_e/m_i)^{1/2} \to 0$, ES structures do not have a large enough spatial extent to be affected by perpendicular-to-the-field shear in IS $\boldsymbol{E} \times \boldsymbol{B}$ flows.

Finally, we note that the scale-separated model should be modified if factors that we have assumed to be of order unity become large enough to interfere with the $(m_e/m_i)^{1/2}$ expansion; possible examples of such parameters include the ratio $(\gamma_{\mathrm{ETG}}/k_{\mathrm{ETG}})/(\gamma_{\mathrm{ITG}}/k_{\mathrm{ITG}})$, the degree of spatial anisotropy in the turbulence, and the ratio of the zonal to non-zonal fluctuation amplitudes (Hardman *et al.* 2019).

Acknowledgements

The authors would like to thank A. A. Schekochihin, W. Dorland, F. I. Parra, P. Dellar, S. C. Cowley, J. Ball, A. Geraldini, N. Christen, A. Mauriya, P. Ivanov, Y. Kawazura, J. Parisi and J. Ruiz Ruiz for useful discussion. This work has been carried out within the framework of the EUROfusion Consortium and has received funding from the Euratom research and training programme 2014–2018 and 2019–2020 under grant agreement No. 633053 and from the RCUK Energy Programme [Grant Numbers EP/P012450/1 and EP/T012250/1]. The views and opinions expressed herein do not necessarily reflect those of the European Commission. This work was supported in part by the Engineering and Physical Sciences Research Council (EPSRC) [Grant Number EP/R034737/1]. The author acknowledges EUROfusion, the EUROfusion High Performance Computer (Marconi-Fusion) under the project MULTEI, the use of ARCHER under the project e607, and the use of ARCHER through the Plasma HEC Consortium EPSRC Grant Numbers EP/L000237/1 and EP/R029148/1 under the projects e281-gs2, software support through the Plasma-CCP Network under EPSRC Grant Number EP/M022463/1 and support from the Wolfgang Pauli Institute. The simulations presented in this work were performed using the GS2 branch https://bitbucket.org/gyrokinetics/gs2/branch/ms_pgelres, with the latest revision at the time of writing being commit ade5780. GS2 input files for the simulations presented in this work may be found at https://doi.org/10.5287/bodleian:b7xOD0P8d.

Editor William Dorland thanks the referees for their advice in evaluating this article.

Declaration of interests

The authors report no conflict of interest.

Appendix A. Simulation resolutions

This appendix details the resolutions used for the simulations presented in this paper.

A.1. *Nonlinear simulations*

For the nonlinear simulations presented in § 3 we use a flux tube with a perpendicular cross-section of $40\pi\rho_{\mathrm{th},i} \times 40\pi\rho_{\mathrm{th},i}$, and a single poloidal turn in the parallel-to-the-field direction. We use $n_y = 21$ toroidal modes with $k_y > 0$ and $k_y^{\max}\rho_{\mathrm{th},i} = 1.05$. We use $n_x = 255$ radial modes with $k_x^{\max}\rho_{\mathrm{th},i} = 6.38$. We specify that each (k_x, k_y) mode has a $[-\pi, \pi]$ extent in θ, with $n_\theta = 33$ points. We use a λ grid with $n_\lambda = 27$. To describe passing particles we take $n_{\lambda,p} = 11$ points, chosen using Gauss–Radau rules (Hildebrand 1987). For the trapped particles we employ a non-spectral, unequally spaced grid in λ, with $n_{\lambda,\mathrm{t}} = 16$ points at the outboard midplane. Following Barnes, Dorland & Tatsuno (2010), we use an ε grid derived from a spectral speed $v = \sqrt{2\varepsilon/m}$ grid with $n_\varepsilon = 12$ points. For the near-marginal nonlinear simulation presented in § 7 we use the resolutions described previously, with $n_\varepsilon = 16$.

A.2. *Linear simulations*

For the linear simulations presented in §§ 3–7 we use ballooning modes with an extent $[-3\pi, 3\pi]$ in the ballooning angle. For compatibility with the nonlinear simulations, each $[-\pi, \pi]$ segment has $n_\theta = 33$ points, and we take $n_\lambda = 27$. For the near-marginal linear simulations presented in § 7, and the linear simulations used to calculate the growth rate $\gamma_{\max}^{\mathrm{CBC}}$ in figure 11(*a*), we take $n_\varepsilon = 16$. For the linear simulations presented in §§ 3–6 (excluding those used to calculate $\gamma_{\max}^{\mathrm{CBC}}$) we take $n_\varepsilon = 12$. For all ES linear simulations

we consider 21 toroidal modes in the wave number range $0.04 \leqslant k_y\rho_{\mathrm{th},e} \leqslant 0.86$ ($2.5 \leqslant k_y\rho_{\mathrm{th},i} \leqslant 52.5$), and we consider 21 values of $\hat{\theta}_0$ in the range $-\pi < \hat{\theta}_0 < \pi$. The growth rate $\gamma_{\max}^{\mathrm{CBC}}$ in figure 11(*a*) is computed for $\hat{\theta}_0 = 0$ and $0.04 \leqslant k_y\rho_{\mathrm{th},e} \leqslant 0.86$.

REFERENCES

ABEL, I. G., PLUNK, G. G., WANG, E., BARNES, M., COWLEY, S. C., DORLAND, W. & SCHEKOCHIHIN, A. A. 2013 Multiscale gyrokinetics for rotating tokamak plasmas: fluctuations, transport, and energy flows. *Rep. Prog. Phys.* **76**, 116201.

ADAM, J. C., TANG, W. M. & RUTHERFORD, P. H. 1976 Destabilization of the trapped-electron mode by magnetic curvature drift resonances. *Phys. Fluids* **19**, 561–566.

BARNES, M., DORLAND, W. & TATSUNO, T. 2010 Resolving velocity space dynamics in continuum gyrokinetics. *Phys. Plasmas* **17**, 032106.

BARNES, M., PARRA, F. I. & SCHEKOCHIHIN, A. A. 2011 Critically balanced ion temperature gradient turbulence in fusion plasmas. *Phys. Rev. Lett.* **107**, 115003.

BONANOMI, N., MANTICA, P., CITRIN, J., GÖRLER, T., TEACA, B. & JET CONTRIBUTORS 2018 Impact of electron-scale turbulence and multi-scale interactions in the JET tokamak. *Nucl. Fusion* **58**, 124003.

BRIZARD, A. J. & HAHM, T. S. 2007 Foundations of nonlinear gyrokinetic theory. *Rev. Mod. Phys.* **79**, 421–468.

CANDY, J., WALTZ, R. E., FAHEY, M. R. & HOLLAND, C. 2007 The effect of ion-scale dynamics on electron-temperature-gradient turbulence. *Plasma Phys. Control. Fusion* **49**, 1209–1220.

CATTO, P. J. 1978 Linearized gyro-kinetics. *Plasma Phys.* **20**, 719–722.

COWLEY, S. C., KULSRUD, R. M. & SUDAN, R. 1991 Considerations of ion-temperature-gradient-driven turbulence. *Phys. Fluids* B **3**, 2767–2782.

CREELY, A. J., RODRIGUEZ-FERNANDEZ, P., CONWAY, G. D., FREETHY, S. J., HOWARD, N. T., WHITE, A. E. & THE ASDEX UPGRADE TEAM 2019 Criteria for the importance of multi-scale interactions in turbulent transport simulations. *Plasma Phys. Control. Fusion* **61**, 085022.

DIMITS, A. M., BATEMAN, G., BEER, M. A., COHEN, B. I., DORLAND, W., HAMMETT, G. W., KIM, C., KINSEY, J. E., KOTSCHENREUTHER, M., KRITZ, A. H., *et al.* 2000 Comparisons and physics basis of tokamak transport models and turbulence simulations. *Phys. Plasmas* **7**, 969–983.

DORLAND, W., JENKO, F., KOTSCHENREUTHER, M. & ROGERS, B. N. 2000 Electron temperature gradient turbulence. *Phys. Rev. Lett.* **85**, 5579–5582.

FRIEMAN, E. A. & CHEN, L. 1982 Nonlinear gyrokinetic equations for low-frequency electromagnetic waves in general plasma equilibria. *Phys. Fluids* **25**, 502–508.

GÖRLER, T. & JENKO, F. 2008 Scale separation between electron and ion thermal transport. *Phys. Rev. Lett.* **100**, 185002.

HARDMAN, M. 2019 Multiscale turbulence in magnetic confinement fusion devices. PhD thesis, University of Oxford.

HARDMAN, M. R., BARNES, M., ROACH, C. M. & PARRA, F. I. 2019 A scale-separated approach for studying coupled ion and electron scale turbulence. *Plasma Phys. Control. Fusion* **61**, 065025.

HILDEBRAND, F. B. 1987 *Introduction to Numerical Analysis*, 2nd edn. Dover.

HORTON, W., HONG, B. G. & TANG, W. M. 1988 Toroidal electron temperature gradient driven drift modes. *Phys. Fluids* **31**, 2971–2983.

HOWARD, N. T., HOLLAND, C., WHITE, A. E., GREENWALD, M. & CANDY, J. 2014 Synergistic cross-scale coupling of turbulence in a tokamak plasma. *Phys. Plasmas* **21**, 112510.

HOWARD, N. T., HOLLAND, C., WHITE, A. E., GREENWALD, M. & CANDY, J. 2015 Fidelity of reduced and realistic electron mass ratio multi-scale gyrokinetic simulations of tokamak discharges. *Plasma Phys. Control. Fusion* **57**, 065009.

HOWARD, N. T., HOLLAND, C., WHITE, A. E., GREENWALD, M. & CANDY, J. 2016*a* Multi-scale gyrokinetic simulation of tokamak plasmas: enhanced heat loss due to cross-scale coupling of plasma turbulence. *Nucl. Fusion* **56**, 014004.

HOWARD, N. T., HOLLAND, C., WHITE, A. E., GREENWALD, M., CANDY, J. & CREELY, A. J. 2016*b* Multi-scale gyrokinetic simulations: comparison with experiment and implications for predicting turbulence and transport. *Phys. Plasmas* **23**, 056109.

ITOH, S.-I. & ITOH, K. 2001 Statistical theory and transition in multiple-scale-length turbulence in plasmas. *Plasma Phys. Control. Fusion* **43**, 1055–1102.

JENKO, F. & DORLAND, W. 2002 Prediction of significant tokamak turbulence at electron gyroradius scales. *Phys. Rev. Lett*. **89**, 225001.

JENKO, F., DORLAND, W., KOTSCHENREUTHER, M. & ROGERS, B. N. 2000 Electron temperature gradient driven turbulence. *Phys. Plasmas* **7**, 1904–1910.

KOTSCHENREUTHER, M., REWOLDT, G. & TANG, W. 1995 Comparison of initial value and eigenvalue codes for kinetic toroidal plasma instabilities. *Comput. Phys. Commun*. **88**, 128–140.

LEE, Y. C., DONG, J. Q., GUZDAR, P. N. & LIU, C. S. 1987 Collisionless electron temperature gradient instability. *Phys. Fluids* **30**, 1331–1339.

MAEYAMA, S., IDOMURA, Y., WATANABE, T.-H., NAKATA, M., YAGI, M., MIYATO, N., ISHIZAWA, A. & NUNAMI, M. 2015 Cross-scale interactions between electron and ion scale turbulence in a tokamak plasma. *Phys. Rev. Lett*. **114**, 255002.

MAEYAMA, S., WATANABE, T.-H., IDOMURA, Y., NAKATA, M., ISHIZAWA, A. & NUNAMI, M. 2017*a* Cross-scale interactions between turbulence driven by electron and ion temperature gradients via sub-ion-scale structures. *Nucl. Fusion* **57**, 066036.

MAEYAMA, S., WATANABE, T.-H. & ISHIZAWA, A. 2017*b* Suppression of ion-scale microtearing modes by electron-scale turbulence via cross-scale nonlinear interactions in tokamak plasmas. *Phys. Rev. Lett*. **119**, 195002.

PARISI, J. F., PARRA, F. I., ROACH, C. M., GIROUD, C., DORLAND, W., HATCH, D. R., BARNES, M., HILLESHEIM, J. C., AIBA, N., BALL, J., *et al.* 2020 Toroidal and slab ETG instability dominance in the linear spectrum of JET-ILW pedestals. *Nucl. Fusion* **60**, 126045.

ROACH, C. M., ABEL, I. G., AKERS, R. J., ARTER, W., BARNES, M., CAMENEN, Y., CASSON, F. J., COLYER, G., CONNOR, J. W., COWLEY, S. C., *et al.* 2009 Gyrokinetic simulations of spherical tokamaks. *Plasma Phys. Control. Fusion* **51**, 124020.

ROGERS, B. N., DORLAND, W. & KOTSCHENREUTHER, M. 2000 Generation and stability of zonal flows in ion-temperature-gradient mode turbulence. *Phys. Rev. Lett*. **85**, 5336–5339.

ROMANELLI, F. 1989 Ion temperature-gradient-driven modes and anomalous ion transport in tokamaks. *Phys. Fluids* B **1**, 1018–1025.

SMITH, S. A. 1997Dissipative closures for statistical moments, fluid moments, and subgrid scales in plasma turbulence. PhD thesis, Princeton University.

STAEBLER, G. M., CANDY, J., HOWARD, N. T. & HOLLAND, C. 2016 The role of zonal flows in the saturation of multi-scale gyrokinetic turbulence. *Phys. Plasmas* **23**, 062518.

STAEBLER, G. M., HOWARD, N. T., CANDY, J. & HOLLAND, C. 2017 A model of the saturation of coupled electron and ion scale gyrokinetic turbulence. *Nucl. Fusion* **57**, 066046.

SUGAMA, H. & HORTON, W. 1997 Transport processes and entropy production in toroidally rotating plasmas with electrostatic turbulence. *Phys. Plasmas* **4**, 405–418.

WALTZ, R. E., CANDY, J. & FAHEY, M. 2007 Coupled ion temperature gradient and trapped electron mode to electron temperature gradient mode gyrokinetic simulations. *Phys. Plasmas* **14**, 056116.